Bubbly flow simulation with particle-center-averaged Euler-Euler model: Fixed polydispersity and bubble deformation

Lyu, H.; Lucas, D.; Rzehak, R.; Schlegel, F.;

Originally published:

December 2022

Chemical Engineering Research and Design 190(2023), 421-433

DOI: https://doi.org/10.1016/j.cherd.2022.12.033

Perma-Link to Publication Repository of HZDR:

https://www.hzdr.de/publications/Publ-35186

Bubbly flow simulation with particle-center-averaged Euler-Euler model: Fixed polydispersity and bubble deformation

Hongmei Lyu*, Dirk Lucas, Roland Rzehak, Fabian Schlegel

Institute of Fluid Dynamics, Helmholtz-Zentrum Dresden-Rossendorf, Bautzner Landstrasse 400, 01328 Dresden

Abstract

Bubble size and deformation are important factors for the closure models required in Euler-Euler simulations of bubbly flows. To properly simulate polydisperse bubbly flows where the bubble size spectrum may cover a range of several millimeters, several velocity groups with different sizes have to be considered. To this end, the theory for the particle-center-averaged Euler-Euler model is generalized for the simulation with multiple bubble velocity groups. Furthermore, bubble deformation effects have been included in appropriate bubble force models. The particle-center-averaged Euler-Euler model provides additional freedom to consider the bubble shape during the conversion between the bubble number density and the gas volume fraction. Therefore, the theory is also generalized to consider an oblate ellipsoidal bubble shape in simulations. A bubbly pipe flow is used to validate the theory and to demonstrate the improvements of the proposed generalizations.

Keywords: fixed polydispersity, bubble deformation, particle-center-averaging method, Euler-Euler model

1. Introduction

In gas-liquid bubbly flows, a spatial point in the fluid domain can be occupied by gas and liquid consecutively. Modeling the local instantaneous characteristic is challenging because of the discontinuity of the fluid properties (e.g. density) across the phase interface, the quantity fluctuations induced by turbulence, and interface motion (Ishii and Hibiki, 2011). Fortunately, detailed flow information, which does not influence the mean flow, is rarely needed for the design of some industrial facilities and processes (Drew, 1983; Ishii and Hibiki, 2011). The fundamental information for the mean fluid motion and properties can be obtained by applying a proper averaging method to the local instantaneous conservation equations to average the small length scales at the phase interface and some fluctuations. This is the motivation for developing an Euler-Euler framework that treats two-phase flow as interpenetrating continua.

After averaging, a set of conservation equations for mass, momentum, and energy is established for each phase. The interfacial interactions and turbulence are represented by closure models, for example, the momentum interactions and Reynolds stresses in momentum equations. With the Euler-Euler model, it is possible to simulate disperse bubbly flow for industrial-scale and complex problems with an affordable computational cost (Drew and Passman, 1998; Ishii and Hibiki, 2011).

The closure models for the interfacial momentum interactions and the bubble-induced turbulence depend on the bubble size. This is particularly important for the shear-lift force,

Email address: hongmeilyu@gmail.com (Hongmei Lyu*)

which pushes small bubbles (with a diameter smaller than 5-6 mm) to the wall, while it drives the large ones to the channel center in case of upward pipe flows (Hessenkemper et al., 2021; Lucas and Tomiyama, 2011; Tomiyama et al., 2002). For monodisperse Euler-Euler simulation, an averaged bubble diameter is used for all the bubbles in the system. This is adequate for flows where the bubbles in the system have a narrow size distribution. For polydisperse bubbly flows, the bubble size spectrum may cover a range of several millimeters. To properly simulate such flows, the bubble size should not be represented by an averaged bubble diameter. Typically, bubble coalescence and breakup also play a role in such flows, however, reliable models for these phenomena are not yet available (Liao et al., 2015). Therefore as an intermediate step, the present contribution does not involve bubble coalescence and breakup, but focuses on simulations with fixed polydispersity. Herein, fixed polydispersity means that the bubble size distribution is assumed to be unchanged throughout the flow.

Bubble deformation is another factor that influences the simulated gas volume fraction distribution. In a clean air-water system, a bubble with an equivalent diameter smaller than 1.3 mm can keep a spherical shape due to the surface tension effects (Jeong and Park, 2015). When the equivalent diameter becomes larger, the bubble shape may turn into an ellipsoid or a spherical cap, depending on the bubble Reynolds number and the bubble size (Grace et al., 1976). For the standard Euler-Euler model, the bubble size and shape influence the distribution of the gas volume fraction by changing the effects of closure models (Hessenkemper et al., 2021). For the particle-center-averaged Euler-Euler model developed by Lyu et al. (2022), the bubble size and shape can also be considered in the conversion between bubble number density and gas volume fraction. Hence, the bubble shape directly affects the gas volume fraction distribution.

This work further develops the particle-center-averaged Euler-Euler model (Lyu et al., 2022, 2020) for fixed polydisperse simulations. Moreover, bubble deformation is considered in simulations by anisotropic diffusion to convert between bubble number density and gas volume fraction. This Euler-Euler approach is implemented based on the solver *multiphaseEulerFoam* in the OpenFOAM Foundation release (The OpenFOAM Foundation Ltd., 2021). To validate the approach, a comparison is made between the simulation results and the experimental data for bubbly pipe flows. The remaining part of this paper is organized as follows: Section 2 summarizes the theory of the particle-center-averaged Euler-Euler model. Besides stating the conservation equations and the method for quantity conversions, the way to consider an oblate ellipsoidal bubble shape in the particle-center-averaged Euler-Euler model by an anisotropic diffusion is introduced and verified. Section 3 describes the experiment from which the measurement data were obtained. The corresponding simulation setups are also introduced. Section 4 presents the comparison between the experimental data and the simulation results. Comparison is made between monodisperse and fixed polydisperse simulations with a varying number of bubble velocity groups as well as bubbles of a spherical and an oblate ellipsoidal shape. The conclusions for the present work are given in Section 5.

2. Particle-center-averaged Euler-Euler model

2.1. Conservation equations

In this study, both phases are taken as incompressible Newtonian fluids. A feature of the particle-center-averaged Euler-Euler model is that the phase-averaging method and the particle-center-averaging method (PCAM) are used to average the solution variables for the continuous and the disperse phase, respectively. The disperse bubbles with a fixed size distribution are divided into one or multiple velocity groups. The simulation with one bubble velocity group is called a monodisperse simulation. For the simulation with multiple bubble

velocity groups, each velocity group has its representative bubble diameter and separate continuity and momentum equations are solved. Hence, each bubble velocity group acts like an independent disperse phase and this simulation is called a fixed polydisperse simulation.

The continuity and momentum equations for the disperse phase in Lyu et al. (2022) and Prosperetti (1998) are generalized by assigning an individual bubble number density to each bubble velocity group. As a result, the continuity equation for each bubble velocity group states

$$\frac{\partial(\beta_{\mathrm{d}i}\rho_{\mathrm{d}i})}{\partial t} + \boldsymbol{\nabla}\cdot(\beta_{\mathrm{d}i}\rho_{\mathrm{d}i}\left\langle \boldsymbol{u}_{\mathrm{d}i}\right\rangle) = 0. \tag{1}$$

Herein, $i = 1, \cdots, N_{\mathrm{g}}$, i is the index of the bubble velocity groups, N_{g} is their number, and the subscript d denotes the disperse phase. In Eq. (1), ρ is the density, t is the physical time, $\boldsymbol{u}$ is the velocity and the notation "$< \cdot >$" indicates the particle-center-averaging. Besides, $\beta_{\mathrm{d}i}$ is the gas volume fraction projecting all the bubble volume to the bubble centers for the bubble velocity group i. It is calculated by

$$\beta_{\mathrm{d}i} = n_{\mathrm{d}i}V_{\mathrm{B}i}, \tag{2}$$

where n is the bubble number density and $V_{\mathrm{B}i}$ is the representative bubble volume of the bubble velocity group i. The gas volume fraction of the bubble velocity group i is denoted as $\alpha_{\mathrm{d}i}$ and the conversion from $\beta_{\mathrm{d}i}$ to $\alpha_{\mathrm{d}i}$ will be introduced in Subsection 2.2. The total gas volume fraction is calculated by

$$\alpha_{\mathrm{d}} = \sum_{i=1}^{N_{\mathrm{g}}}\alpha_{\mathrm{d}i}. \tag{3}$$

The disperse phase velocity is calculated by

$$\left\langle \boldsymbol{u}_{\mathrm{d}}\right\rangle = \sum_{i=1}^{N_{\mathrm{g}}}\frac{\alpha_{\mathrm{d}i}}{\alpha_{\mathrm{d}}}\left\langle \boldsymbol{u}_{\mathrm{d}i}\right\rangle. \tag{4}$$

For the continuous phase, the continuity equation is

$$\frac{\partial(\alpha_{\mathrm{c}}\rho_{\mathrm{c}})}{\partial t} + \boldsymbol{\nabla}\cdot(\alpha_{\mathrm{c}}\rho_{\mathrm{c}}\overline{\boldsymbol{u}_{\mathrm{c}}}) = 0, \tag{5}$$

where α_{c} is the liquid volume fraction, the overbar "$\overline{\cdot}$" indicates the phase-averaging, and the subscript c denotes the continuous phase. The volume fractions for both phases fulfill

$$\alpha_{\mathrm{d}} + \alpha_{\mathrm{c}} = 1. \tag{6}$$

The particle-center-averaged momentum equation for each bubble velocity group reads

$$\begin{aligned}&\frac{\partial(\beta_{\mathrm{d}i}\rho_{\mathrm{d}i}\left\langle \boldsymbol{u}_{\mathrm{d}i}\right\rangle)}{\partial t} + \boldsymbol{\nabla}\cdot(\beta_{\mathrm{d}i}\rho_{\mathrm{d}i}\left\langle \boldsymbol{u}_{\mathrm{d}i}\right\rangle\left\langle \boldsymbol{u}_{\mathrm{d}i}\right\rangle)\\ &= -\beta_{\mathrm{d}i}\nabla\overline{p_{\mathrm{c}}} + \beta_{\mathrm{d}i}\boldsymbol{\nabla}\cdot\overline{\mathbf{S}_{\mathrm{c}}} + \boldsymbol{\nabla}\cdot(\beta_{\mathrm{d}i}\left\langle \mathbf{T}_{\mathrm{d}i}\right\rangle) + \left\langle \boldsymbol{f}_{\mathrm{d}i}\right\rangle + \beta_{\mathrm{d}i}\rho_{\mathrm{d}i}\boldsymbol{g}.\end{aligned} \tag{7}$$

Herein, p, $\mathbf{S}$, $\mathbf{T}$, $\boldsymbol{f}$, and $\boldsymbol{g}$ are the pressure, the viscous stress tensor, the Reynolds stress tensor, the force per unit volume, and the acceleration of gravity, respectively. The momentum equation for the continuous phase states

$$\begin{aligned}&\frac{\partial(\alpha_{\mathrm{c}}\rho_{\mathrm{c}}\overline{\boldsymbol{u}_{\mathrm{c}}})}{\partial t} + \boldsymbol{\nabla}\cdot(\alpha_{\mathrm{c}}\rho_{\mathrm{c}}\,\overline{\boldsymbol{u}_{\mathrm{c}}}\,\overline{\boldsymbol{u}_{\mathrm{c}}})\\ &= -\alpha_{\mathrm{c}}\nabla\overline{p_{\mathrm{c}}} + \alpha_{\mathrm{c}}\boldsymbol{\nabla}\cdot\overline{\mathbf{S}_{\mathrm{c}}} + \boldsymbol{\nabla}\cdot(\alpha_{\mathrm{c}}\overline{\mathbf{T}_{\mathrm{c}}}) + \overline{\boldsymbol{f}_{\mathrm{c}}} + \alpha_{\mathrm{c}}\rho_{\mathrm{c}}\boldsymbol{g}.\end{aligned} \tag{8}$$

2.2. Quantity conversions

As shown in Subsection 2.1, the solution variables for the disperse and the continuous phase are particle-center-averaged and phase-averaged quantities, respectively. During the solution process, a way to convert these quantities is required. In this study, the transformation from particle-center-averaged to phase-averaged quantities in three-dimensional space is established by the following Gaussian convolution:

$$\overline{\Phi}(\boldsymbol{x},\tau)=\int_{\Omega}\langle\Phi\rangle\left(\boldsymbol{x}_0\right)\frac{1}{\left(4\pi C_{\mathrm{diff}}\tau\right)^{\frac{3}{2}}}\exp\left[-\frac{\left(\boldsymbol{x}-\boldsymbol{x}_0\right)^2}{4C_{\mathrm{diff}}\tau}\right]\mathrm{d}\boldsymbol{x}_0, \tag{9}$$

where Φ denotes the quantity for conversion, $\boldsymbol{x}$ and $\boldsymbol{x}_0$ are spatial coordinate vectors, and Ω is the fluid domain, while τ and C_{diff} are the diffusion pseudo-time and the diffusion coefficient, respectively.

In this way, the conversion between $\beta_{\mathrm{d}i}$ and $\alpha_{\mathrm{d}i}$ is realized by

$$\alpha_{\mathrm{d}i}(\boldsymbol{x},\tau)=\int_{\Omega}\beta_{\mathrm{d}i}\left(\boldsymbol{x}_0\right)\frac{1}{\left(4\pi C_{\mathrm{diff}}\tau\right)^{\frac{3}{2}}}\exp\left[-\frac{\left(\boldsymbol{x}-\boldsymbol{x}_0\right)^2}{4C_{\mathrm{diff}}\tau}\right]\mathrm{d}\boldsymbol{x}_0. \tag{10}$$

Similarly, the force for the disperse phase is transferred to the force for the continuous phase with

$$\overline{\boldsymbol{f}_{\mathrm{c}}}(\boldsymbol{x},\tau)=-\sum_{i=1}^{N_g}\int_{\Omega}\langle\boldsymbol{f}_{\mathrm{d}i}\rangle\left(\boldsymbol{x}_0\right)\frac{1}{\left(4\pi C_{\mathrm{diff}}\tau\right)^{\frac{3}{2}}}\exp\left[-\frac{\left(\boldsymbol{x}-\boldsymbol{x}_0\right)^2}{4C_{\mathrm{diff}}\tau}\right]\mathrm{d}\boldsymbol{x}_0. \tag{11}$$

The phase-averaged gas velocity is also calculated from the particle-center-averaged gas velocity by

$$\overline{\boldsymbol{u}_{\mathrm{d}i}}(\boldsymbol{x},\tau)=\frac{1}{\alpha_{\mathrm{d}i}(\boldsymbol{x},\tau)}\int_{\Omega}\beta_{\mathrm{d}i}\left(\boldsymbol{x}_0\right)\langle\boldsymbol{u}_{\mathrm{d}i}\rangle\left(\boldsymbol{x}_0\right)\frac{1}{\left(4\pi C_{\mathrm{diff}}\tau\right)^{\frac{3}{2}}}\exp\left[-\frac{\left(\boldsymbol{x}-\boldsymbol{x}_0\right)^2}{4C_{\mathrm{diff}}\tau}\right]\mathrm{d}\boldsymbol{x}_0. \tag{12}$$

Implementing these Gaussian convolutions directly in OpenFOAM code which is based on unstructured grids is difficult and can be computationally costly. As an alternative, this study realizes the Gaussian convolutions of Eq. (9) by solving the following diffusion equation:

$$\frac{\partial\overline{\Phi}}{\partial\tau}-\boldsymbol{\nabla}\cdot\left(C_{\mathrm{diff}}\nabla\overline{\Phi}\right)=0, \tag{13}$$

with an initial condition of $\overline{\Phi}\left(\boldsymbol{x_0},0\right)=\langle\Phi\rangle\left(\boldsymbol{x_0}\right)$. Sun and Xiao (2015) illustrated that solving Eq. (13) together with the initial condition is equivalent to using the Gaussian convolution. In this study, the diffusion coefficient C_{diff} is set to $1\,\mathrm{m^2\,s^{-1}}$ for the spherical bubbles. An optimized value for τ, which is $0.03356\,d_{\mathrm{B}}^2/C_{\mathrm{diff}}$, is determined by Lyu et al. (2022). Herein, d_{B} is the bubble diameter. Hence, the optimized τ for the bubble velocity group i is $0.03356\,d_{\mathrm{B}i}^2/C_{\mathrm{diff}}$, where $d_{\mathrm{B}i}$ is the representative bubble diameter for the velocity group.

2.3. Treatment of bubble deformation

Use of a scalar diffusion coefficient C_{diff} in Eq. (13) implies that the diffusion is isotropic, which is suitable for spherical bubbles. For a deformed bubble, the diffusion of the bubble volume from the bubble's center of mass should be anisotropic, so the diffusion coefficient becomes a tensor $\mathbf{C}_{\mathrm{diff}}$. In the following, the relation between the bubble shape and the diffusion tensor will be established.

After the bubble volume being diffused from the bubble's center-of-mass location ($\boldsymbol{x} = \mathbf{0}$) for certain time τ, the gas volume fraction distribution a can be expressed as (Basser, 1995)

$$\alpha_{\mathrm{d}}(\boldsymbol{x}, \tau) = \frac{V_{\mathrm{B}}}{\sqrt{|\mathbf{C}_{\mathrm{diff}}|(4\pi\tau)^3}} \exp\left(\frac{-\boldsymbol{x}^{\mathrm{T}}{\mathbf{C}_{\mathrm{diff}}}^{-1}\boldsymbol{x}}{4\tau}\right). \tag{14}$$

The isosurface of $\alpha_{\mathrm{d}}(\boldsymbol{x}, \tau)$ forms a sphere for isotropic diffusion, which is called *diffusion sphere*. In comparison, it can be an ellipsoid for anisotropic diffusion, which is called *diffusion ellipsoid*. If the axes of the diffusion ellipsoid are aligned with the axes of the laboratory frame of reference (x, y, z), only the diagonal components of $\mathbf{C}_{\mathrm{diff}}$ are non-zero. Hence, the isosurface is expressed by (Basser, 1995)

$$\frac{x^2}{C_{\mathrm{diff,\,xx}}\tau} + \frac{y^2}{C_{\mathrm{diff,\,yy}}\tau} + \frac{z^2}{C_{\mathrm{diff,\,zz}}\tau} = 1. \tag{15}$$

The diffusion ellipsoid should have a similar shape, the same orientation and center location as the oblate ellipsoidal bubble. Therefore, if we assume the minor axis of the diffusion ellipsoid along the main flow direction (z axis), we obtain

$$C_{\mathrm{diff,\,xx}} = C_{\mathrm{diff,\,yy}}, \tag{16}$$

and

$$C_{\mathrm{diff,\,xx}} = \chi^2 C_{\mathrm{diff,\,zz}}. \tag{17}$$

Herein, χ is the aspect ratio. The model for χ proposed by Ziegenhein and Lucas (2019) is employed in this study. It has the following form:

$$\chi = 1 + 0.65Eo^{0.35}, \tag{18}$$

where Eo is the Eötvös number, which is defined by

$$Eo = \frac{\Delta\rho|\boldsymbol{g}|d_{\mathrm{B}}^2}{\sigma}. \tag{19}$$

Herein, $\Delta\rho = \rho_{\mathrm{c}} - \rho_{\mathrm{d}}$ and σ is the surface tension coefficient.

The volume of the diffusion ellipsoid for the oblate ellipsoidal bubble should be the same as the diffusion sphere for the spherical bubble. Consequently, we have

$$C_{\mathrm{diff,\,xx}}C_{\mathrm{diff,\,yy}}C_{\mathrm{diff,\,zz}} = 1\ \mathrm{m^6\,s^{-3}}. \tag{20}$$

Based on Eqs. (16), (17), and (20), we derive the components of the diffusion tensor for the oblate ellipsoidal bubbles as: $C_{\mathrm{diff,\,xx}} = C_{\mathrm{diff,\,yy}} = \chi^{\frac{2}{3}}\ \mathrm{m^2\,s^{-1}}$ and $C_{\mathrm{diff,\,zz}} = \chi^{-\frac{4}{3}}\ \mathrm{m^2\,s^{-1}}$.

In the present study, the computational domain in the simulations of bubbly pipe flows for validation is a narrow sector of the test-section pipe because the flow in the location where the simulation results are compared with the experimental data is regarded as circumferentially symmetric. A quasi-two-dimensional mesh is used for the computational domain. Therefore, the diffusion only appears in the radial (x axis) and the axial (z axis) direction, which is two-dimensional. In this condition, Eq. (14) is changed to be (Painter and Hillen, 2013)

$$\alpha_{\mathrm{d}}(\boldsymbol{x}, \tau) = \frac{d_{\mathrm{B}}^2}{16\tau\sqrt{|\mathbf{C}_{\mathrm{diff}}|}} \exp\left(\frac{-\boldsymbol{x}^{\mathrm{T}}{\mathbf{C}_{\mathrm{diff}}}^{-1}\boldsymbol{x}}{4\tau}\right). \tag{21}$$

The equation for the isoline of $\alpha_{\mathrm{d}}(\boldsymbol{x}, \tau)$ is

$$\frac{x^2}{C_{\mathrm{diff,\,xx}}\tau} + \frac{z^2}{C_{\mathrm{diff,\,zz}}\tau} = 1. \tag{22}$$

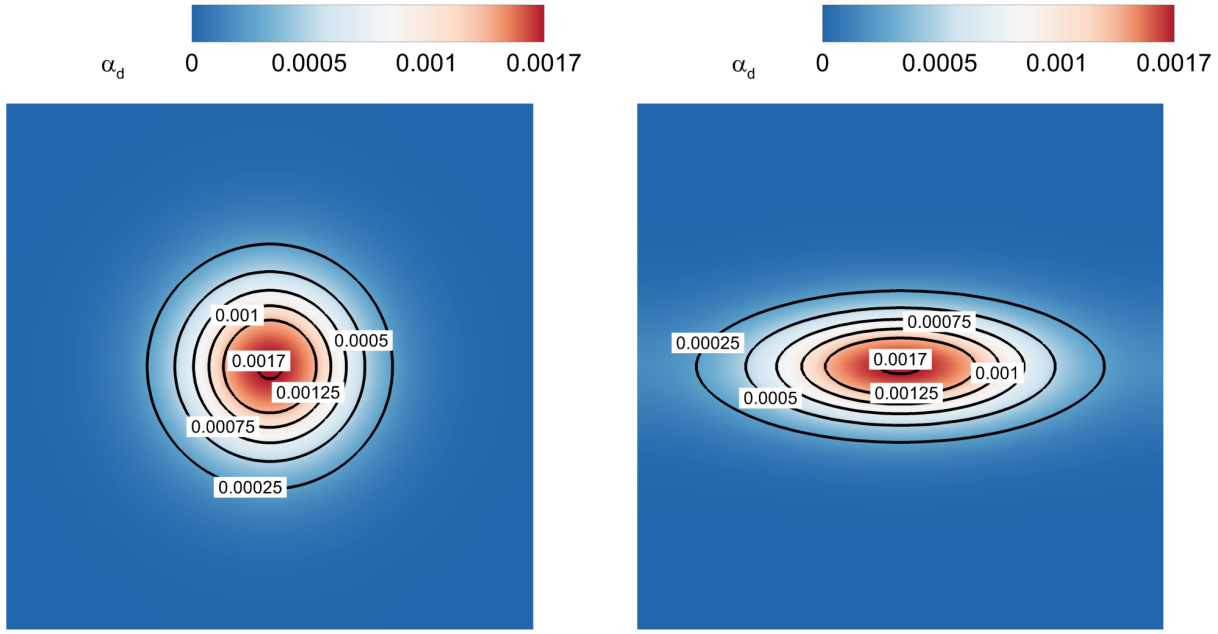

(a) Spherical shape.

(b) Oblate ellipsoidal shape.

Figure 1: Gas volume fraction distribution simulated with different bubble shapes.

The isoline forms a circle for isotropic diffusion or forms an ellipse for anisotropic diffusion, which are named *diffusion circle* and *diffusion ellipse*, respectively. For the diffusion ellipse, the aspect ratio should equal χ. Therefore, the relation between $C_{\mathrm{diff},\,\mathrm{xx}}$ and $C_{\mathrm{diff},\,\mathrm{zz}}$ still fits Eq. (17).

The area of the diffusion circle and the diffusion ellipse should be the same. Consequently, we obtain

$$C_{\mathrm{diff},\,\mathrm{xx}} C_{\mathrm{diff},\,\mathrm{zz}} = 1\ \mathrm{m}^4\,\mathrm{s}^{-2}. \tag{23}$$

Basing on Eqs. (17) and (23), we have $C_{\mathrm{diff},\,\mathrm{xx}} = \chi\ \mathrm{m}^2\,\mathrm{s}^{-1}$ and $C_{\mathrm{diff},\,\mathrm{zz}} = \chi^{-1}\ \mathrm{m}^2\,\mathrm{s}^{-1}$. Equation (23), which is the second constraint used to calculate the diffusion tensor for a two-dimensional case, is different from that for a three-dimensional case (Eq. (20)). Therefore, when applying the theory, the diffusion tensor should be chosen according to the simulation geometry.

A simplified two-dimensional test case is used to verify the method of bubble deformation treatment. The fluid domain is a square with a size of $0.02\,\mathrm{m} \times 0.02\,\mathrm{m}$. In the simulation, both air and water are at rest. Only the process of diffusing the bubble volume from the bubbles' centers of mass was simulated. The bubble diameter is 10 mm. The number of cells is 81×81, and the cell spacing is uniform. The initial value for β_d in the center cell is 1, and it is 0 in the other cells. Figure 1 gives the gas volume fraction distributions and the isolines simulated with different bubble shapes. For the spherical bubble shape, each isoline forms a circle. In comparison, for the oblate ellipsoidal bubble shape, each isoline forms an ellipse. The orientation of the ellipse is as expected. Furthermore, the area of the ellipse is close to that of the corresponding circle. These results prove that the method of bubble deformation treatment works as expected.

2.4. Modeling of bubble forces and turbulence

In the Euler-Euler model, the momentum interactions between the disperse and the continuous phase are usually assumed to be represented by a linear combination of several bubble forces (Ishii and Hibiki, 2011). In this study, the selected closure models for the

Table 1: HZDR baseline model for bubbly flow simulations.

Force and turbulence	Selected model
Drag force	Ishii and Zuber (1979)
Shear-lift force	Hessenkemper et al. (2021) with cosine wall damping
Turbulent dispersion force	Burns et al. (2004)
Wall-lift force	Hosokawa et al. (2002)
Virtual mass force	Constant coefficient, $C_{\mathrm{VM}} = 0.5$ (Auton et al., 1988)
Shear-induced turbulence	$k-\omega$ SST (Menter, 2009)
Bubble-induced turbulence	Ma et al. (2017)

standard Euler-Euler simulations are based on the Helmholtz-Zentrum Dresden-Rossendorf (HZDR) baseline model shown in Table 1 (Hänsch et al., 2021; Rzehak et al., 2017). For the Euler-Euler model based on PCAM, besides the HZDR baseline model, a wall-contact force is required to avoid the bubbles' centers of mass coming non-physically close to the wall. Hence, the wall-contact force model proposed by Lucas et al. (2007) is changed for bubbles with an oblate ellipsoidal shape by Lyu et al. (2022) and the resulting wall-contact force model reads

$$\left\langle \boldsymbol{f}_{\mathrm{d}i}^{\mathrm{WC}} \right\rangle = -\pi d_{\mathrm{B}i}\sigma n_{\mathrm{d}i} \left\{ -\frac{1}{\widetilde{L}^2} + \frac{3\widetilde{L}}{2G}\left[\left(\frac{4\sqrt{G}}{3} + \frac{\widetilde{L}^3}{\sqrt{G}} \right) \operatorname{arctanh}\sqrt{G} - 1 \right] \right\} \boldsymbol{n}_{\mathrm{w}}. \tag{24}$$

Herein, $\widetilde{L} = 2L/d_{\mathrm{B}i}$ and $G = 1 - \widetilde{L}^3$. Besides, L is the distance between the bubble's center of mass and the wall, and $\boldsymbol{n}_{\mathrm{w}}$ is the unit wall-normal vector pointing into the fluid.

Due to the small spatial scales of the disperse phase in bubbly flows, it is sufficient to consider only the turbulence of the continuous phase (Rzehak et al., 2017) and the SST model of Menter (2009) is an appropriate choice. The effects of bubble-induced turbulence are considered as additional source terms in the turbulence model (Ma et al., 2017).

3. Experimental condition and simulation setup

3.1. Description of the experiment

The experimental data obtained from the measurement test loop (MTLoop) facility (Lucas et al., 2005; Prasser et al., 2003) are employed for the validation. In the experiment, a co-current air-water flow in a vertical pipe with an inner diameter of 51.2 mm and a height of 3.5 m was investigated. Water with a temperature of 303.15 K was supplied to the test section by a circulation pump, while pressurized air was injected into the test section by distributed nozzles at the bottom of the test section. The bubble characteristics, including local gas volume fraction, bubble size, and axial bubble velocity, were obtained at several axial heights by wire-mesh sensors with two measurement planes. The data obtained at an axial height of 3.03 m will be compared with the simulation results. The parameters for the selected cases are listed in Table 2. These cases are chosen because they have a relatively low gas volume fraction, which is suitable for simulations with fixed polydispersity. The analysis of fixed polydispersity is based on cases MT40, MT42 and MT86, while cases MT20, MT42, MT64 and MT86 are employed in the study of bubble deformation.

Figure 2 shows the bubble size distributions at different axial levels obtained in the experiment for cases MT40, MT42, and MT86. The bubble size near the inlet is small and it increases downstream due to bubble coalescence and the decrease of local pressure. Meanwhile, the bubble size spectrum downstream covers a larger range than that at the inlet. For case MT86, the bubble size distribution at level $z = 3.03$ m is regarded as fully-developed

Table 2: Parameters for the selected cases (J: superficial velocity).

Name	J_c [m s^{-1}]	J_d [m s^{-1}]	α_d% [-]	d_B [mm]
MT20	1.611	0.004	0.23	3.48
MT40	0.641	0.0096	1.09	5.06
MT42	1.611	0.0096	0.53	3.89
MT64	1.611	0.0235	1.25	4.40
MT86	1.611	0.0574	2.86	4.99

because it matches the distribution at level $z = 2.53$ m. Unfortunately, the measurement bubble size distributions for cases MT40 and MT42 at level $z = 2.53$ m are not available. For both cases, the profiles for the bubble size distributions at levels $z = 3.03$ m and $z = 1.53$ m have a similar shape and their difference is not significant. Therefore, it is speculated that the bubble size distributions at level $z = 3.03$ m for both cases are close to fully-developed. Consequently, it is reasonable to fix the bubble size distribution for simulations with the measurement data at level $z = 3.03$ m.

3.2. Simulation setup

For case MT20, almost all the bubbles have a diameter smaller than 5.2 mm. In this size range, the shear-lift force has the same direction (pointing to the wall). Hence, only one bubble velocity group is used in the simulations. For case MT64, the monodisperse simulation results are almost the same as those using four bubble velocity groups. Therefore, only the monodisperse results are shown here. For the other cases, both monodisperse simulations and fixed polydisperse simulations with a varying number of bubble velocity groups are performed. The bubble sizes for the monodisperse simulations are found in Table 2. The setup for the fixed polydisperse simulations is discussed below.

The computational domain for the steady-state simulations is a small sector of the test section pipe with a center angle of 1° (Fig. 3). The radius (25.6 mm) of the rotationally symmetric domain is the same as the test section pipe. The axial length is 3.5 m, which is beyond the measurement location at $z = 3.03$ m. This avoids a possible influence of the outlet boundary on the simulation results at the measurement location. The simulation results at $z = 3.03$ m are fully-developed. The boundary condition at the pipe wall is a slip boundary for the disperse phase velocity, but a no-slip boundary for the continuous phase velocity.

For monodisperse simulations, at the inlet, by assuming a vanishing relative velocity between the disperse and the continuous phase, the axial velocities are calculated by

$$u_d = u_c = J_d + J_c. \tag{25}$$

The lateral velocity components at the inlet are assumed to be zero. The inlet gas volume fraction is computed by

$$\alpha_d = \frac{J_d}{J_d + J_c}. \tag{26}$$

For the Euler-Euler simulations based on PCAM, at the inlet, the particle-center-averaged velocity is assumed to be the same as the corresponding phase-averaged velocity. In addition, at the inlet, the following relation is assumed:

$$\beta_d = \alpha_d. \tag{27}$$

For fixed polydisperse simulations, bubbles are divided into two to four velocity groups. The critical diameter for the shear-lift coefficient to change its sign (about 5.2 mm) is used

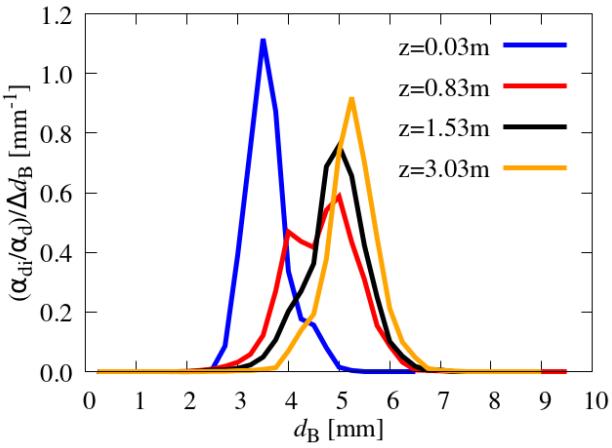

(a) MT40.

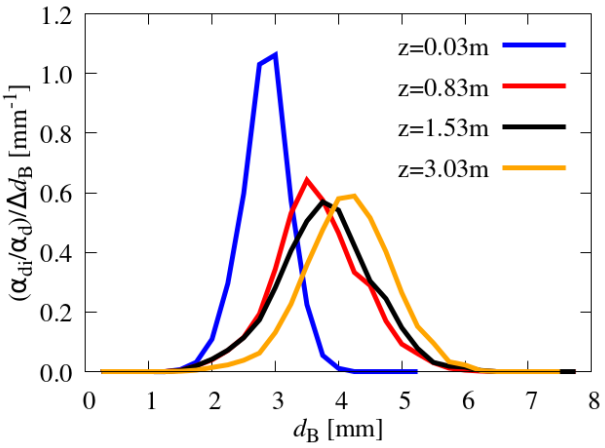

(b) MT42.

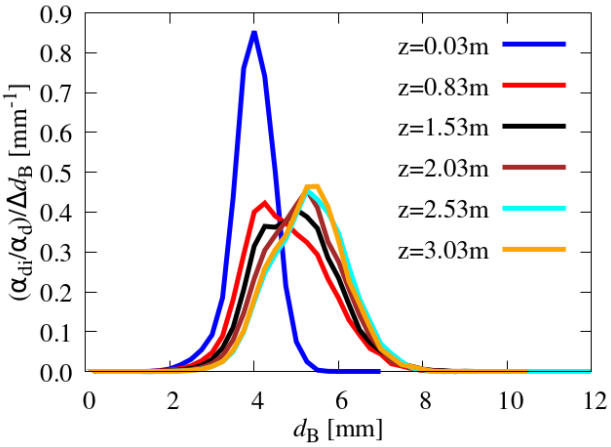

(c) MT86.

Figure 2: Measurement bubble size distribution at different axial heights (Level $z = 0$ m: the axial location of gas injection).

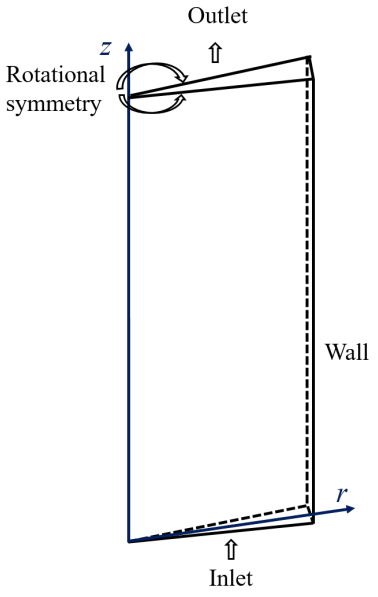

Figure 3: Computational domain and boundary settings in simulations.

Table 3: Parameters for fixed polydisperse simulations.

Name	d_{B1} [mm]	d_{B2} [mm]	d_{B3} [mm]	d_{B4} [mm]	f_{v1}% [-]	f_{v2}% [-]	f_{v3}% [-]	f_{v4}% [-]
2 velocity groups								
MT40	4.77	5.60	-	-	61.7	38.3	-	-
MT42	3.85	5.52	-	-	96.1	3.9	-	-
MT86	4.43	5.87	-	-	54.0	46.0	-	-
3 velocity groups								
MT42	2.55	4.00	5.52	-	6.9	89.2	3.9	-
4 velocity groups								
MT40	2.63	4.78	5.60	7.13	0.2	61.5	38.2	0.1
MT86	2.64	4.47	5.82	7.33	0.6	53.4	44.2	1.8

as a boundary in the division of the velocity groups to allow bubbles to move in various directions. For the simulations using two bubble velocity groups, the bubble size ranges are $0\,\text{mm} < d_B \leq 5.2\,\text{mm}$ and $d_B > 5.2\,\text{mm}$. If four bubble velocity groups are used, the bubble size ranges are $0\,\text{mm} < d_B \leq 3.0\,\text{mm}$, $3.0\,\text{mm} < d_B \leq 5.2\,\text{mm}$, $5.2\,\text{mm} < d_B \leq 7.0\,\text{mm}$ and $d_B > 7.0\,\text{mm}$. For the simulations using three bubble velocity groups, the last two bubble size ranges are merged.

The measurement bubble size distribution at level $z = 3.03\,\text{m}$ is used to calculate the parameters of the disperse phase required in the simulation setup. For the selected cases, the calculated volumetric flow rate fraction (f_{vi}) and representative bubble diameter for each bubble velocity group (d_{Bi}) are listed in Table 3. At the inlet, the cross-sectional distributions of velocities and volume fractions are also assumed to be uniform. The inlet axial velocity of each bubble velocity group is assumed to be the same as the inlet axial velocity of the disperse phase for monodisperse simulations calculated by Eq. (25). The inlet gas volume fraction of the bubble velocity group i is calculated by

$$\alpha_{di} = f_{vi}\alpha_d. \tag{28}$$

Herein, α_d is calculated by Eq. (26).

The computational domain is divided into computational cells by a quasi-two-dimensional mesh with one layer of cells in the circumferential direction. The numbers of cells in the radial and axial directions are 50 and 800, respectively. The cell spacing is uniform in both directions. The simulation results with this mesh resolution are mesh-independent (Lyu, 2022).

The conservation equations and the diffusion equations for the quantity conversions are discretized by a cell-centered finite volume method. Linear interpolation is used to calculate the quantities in the cell face center from the cell center values. For the discretization of the convection term, a flux-limiter is used to make the simulations stable. A first-order Euler implicit scheme is used for temporal discretization. For the discretization of the Laplacian term, linear interpolation is also used to compute the surface normal gradient in the cell face.

4. Comparison between simulation results and experimental data

4.1. Effects of fixed polydispersity

The gas volume fraction simulated with the standard Euler-Euler model and the Euler-Euler model based on PCAM using different numbers of bubble velocity groups are shown

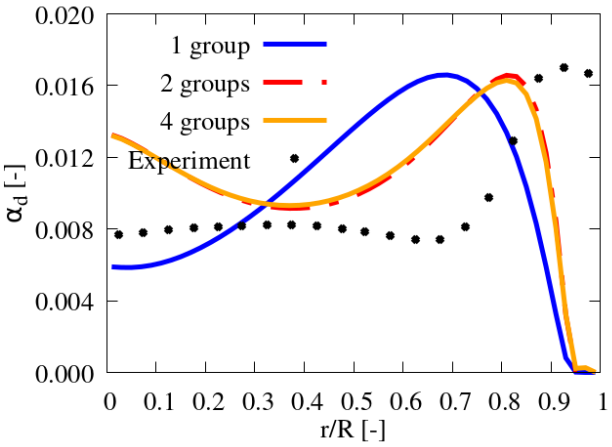

(a) MT40, standard Euler-Euler model.

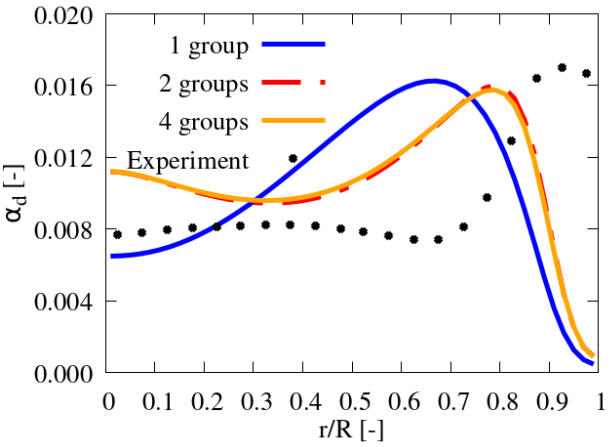

(b) MT40, Euler-Euler model based on PCAM.

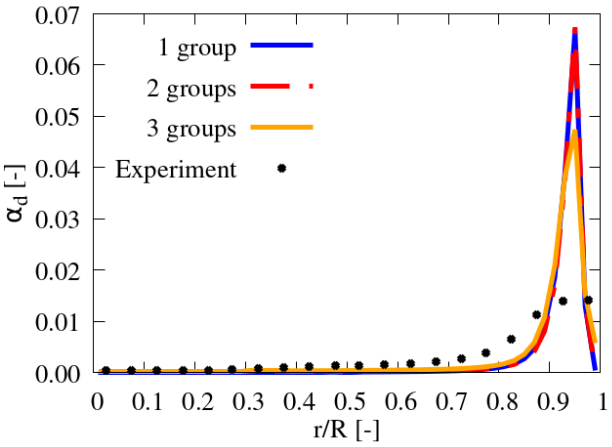

(c) MT42, standard Euler-Euler model.

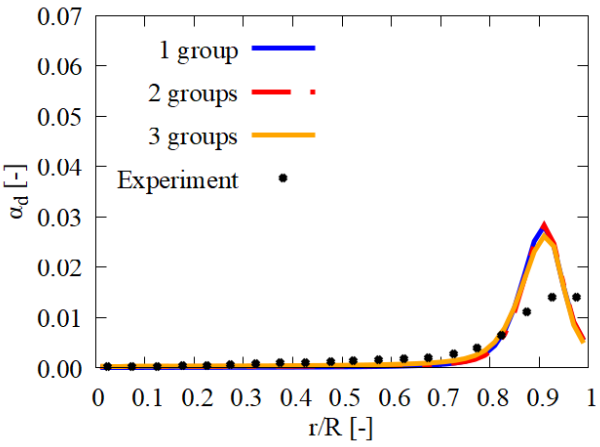

(d) MT42, Euler-Euler model based on PCAM.

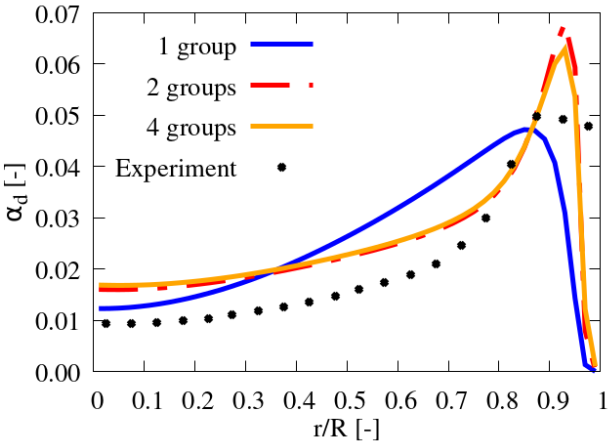

(e) MT86, standard Euler-Euler model.

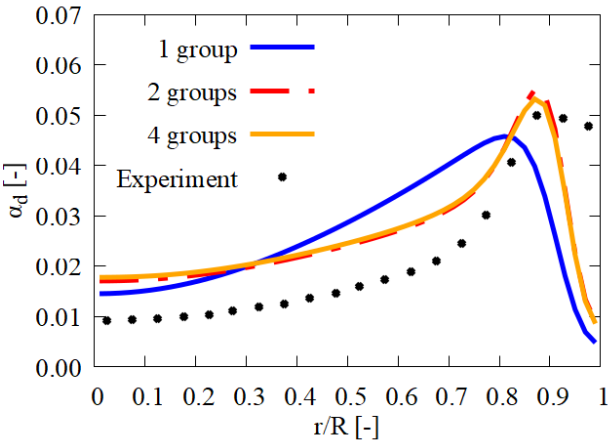

(f) MT86, Euler-Euler model based on PCAM.

Figure 4: Sensitivity of bubble velocity groups.

in Fig. 4 in comparison with the experimental data. Herein, r is the radial coordinate and R is the pipe radius. The monodisperse simulation results are labeled by "1 group".

For case MT40, the gas volume fraction profiles simulated with both Euler-Euler models using one bubble velocity group are wall-peaking, but the peaks are located further away from the wall than the peak in the experimental data. Besides, the small central peak in the experimental data is not reproduced in the simulations. This reason is that using one bubble velocity group with a fixed bubble size cannot reproduce the bubble movements in the experiment in which the bubbles have different sizes and move in different directions. After allowing the bubbles to move in different directions in the simulations by using two bubble velocity groups, the simulated gas volume fraction profiles have a wall peak that is located closer to the experimental data and a central peak that is over-predicted. After using PCAM, the over-prediction of the central peak is slightly alleviated.

For both Euler-Euler models, the gas volume fraction of case MT40 simulated using four bubble velocity groups is almost the same as that simulated with two bubble velocity groups. The deviation between the simulation results with four bubble velocity groups and the experimental data is still obvious. This may result from insufficiencies in the lateral force models used in the simulations and the measurement uncertainty in the experimental data.

For case MT42, the gas volume fraction peaks simulated with the standard Euler-Euler model are over-predicted. The reason is that the shear-lift and the wall-lift force are functions of the local gas volume fraction. Hence, they drive the gas to the peak without considering the bubble spatial extension when the bubble diameter is larger than the computational cell spacing. After using PCAM in the Euler-Euler model, the over-estimation of the gas volume fraction peak is alleviated.

For both Euler-Euler models, the gas volume fraction of case MT42 simulated with two bubble velocity groups matches that simulated with one bubble velocity group. After using three bubble velocity groups, the peak of the gas volume fraction profile simulated with the standard Euler-Euler model becomes lower and slightly wider. In comparison, for the Euler-Euler model based on PCAM, the gas volume fraction simulated with three bubble velocity groups is close to that simulated with one or two bubble velocity groups.

The difference in the simulation results of both Euler-Euler models also comes from the bubble forces. When increasing the number of bubble velocity groups from two to three, the bubble velocity group with a representative diameter of 3.85 mm and a gas volumetric flow rate fraction of 96.1% is divided into two bubble velocity groups. One of them has a representative diameter of 2.55 mm and a gas volumetric flow rate fraction of 6.9%. The other has a representative diameter of 4.00 mm and a gas volumetric flow rate fraction of 89.2%. Hence, the majority of the bubbles experience a lower shear-lift force after using three bubble velocity groups because the shear-lift force coefficient decreases with the increasing bubble size (Fig. 5). Hence, the over-prediction of the gas volume fraction peak for the standard Euler-Euler model also decreases. For the Euler-Euler model based on PCAM, the bubble forces are functions of the bubble number density, which avoids the over-prediction of gas volume fraction caused by the inconsistency of bubble force models. Consequently, the simulated gas volume fractions are less sensitive to the number of bubble velocity groups.

For case MT86, the gas volume fractions simulated with both Euler-Euler models using one bubble velocity group are higher than the measurement data except for the region near the wall. After using two bubble velocity groups, bubbles can move in different directions, so more gas is transported to the near-wall region and the pipe-center region. The peak of the gas volume fraction comes closer to the wall than the peak simulated with one bubble velocity group. The peak is over-predicted by the standard Euler-Euler model. This is because the bubble diameter in the simulation using one bubble velocity group is 4.99 mm, which is close to the critical bubble diameter (about 5.2 mm) for the shear-lift coefficient to

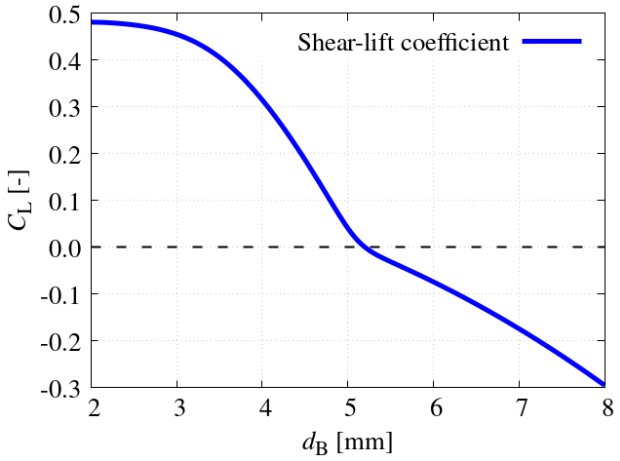

Figure 5: Shear-lift coefficient (C_L) dependency on bubble diameter in air-water system for the model of Hessenkemper et al. (2021).

change its sign (Fig. 5). Therefore, the shear-lift force is relatively small. After dividing the bubbles into two velocity groups, one of the groups has a representative diameter of 4.43 mm and a gas volumetric flow rate fraction of 54.0%. The other group has a representative diameter of 5.87 mm. Consequently, the division decreases the diameter of the bubbles that form the wall peak. As a result, the shear-lift force of the bubbles increases, which leads to a more significant over-prediction of the gas volume fraction peak for the standard Euler-Euler model.

After using PCAM in the Euler-Euler simulation, the over-prediction is alleviated and the simulated gas volume fraction peak agrees well with the peak in the experimental data. For both Euler-Euler models, the gas volume fractions simulated with four bubble velocity groups are approximately the same as those simulated with two bubble velocity groups.

4.2. Effects of bubble deformation

In the Euler-Euler model based on PCAM, bubble deformation can be considered in the conversions between phase-averaged and particle-center-averaged quantities. In Subsection 4.1, the bubble shape is assumed to be spherical. A way to consider an oblate ellipsoidal bubble shape in quantity conversions has been described and verified in Subsection 2.3. In this subsection, the bubble shape effects on the simulation results of the Euler-Euler model based on PCAM are presented and analyzed.

Figure 6 gives the comparison of the measurement data and the gas volume fractions for monodisperse simulations with different bubble shapes. The peak of the gas volume fraction profiles simulated with the oblate ellipsoidal bubble shape is lower and wider than that simulated with the spherical bubble shape. The reason is that the oblate ellipsoidal bubble has a larger extension in the radial direction than the spherical bubble.

As a result, for all cases, the over-prediction of the gas volume fraction peak is alleviated after considering the oblate ellipsoidal bubble shape in the simulations. In the results simulated with the spherical bubble shape, the peak ratio ($\alpha^{\mathrm{sim}}_{\mathrm{d,\,max}}/\alpha^{\mathrm{exp}}_{\mathrm{d,\,max}}$) of the gas volume fraction profile is about 2.12, 1.99, and 1.55 for cases MT20, MT42, and MT64, respectively. Herein, $\alpha^{\mathrm{sim}}_{\mathrm{d,\,max}}$ and $\alpha^{\mathrm{exp}}_{\mathrm{d,\,max}}$ are the maximum gas volume fraction in the simulation results and the experimental data, respectively. By contrast, the ratio decreases to be around 1.59, 1.59, and 1.30 for the profile simulated with the oblate ellipsoidal bubble shape. Near the wall with $0.92 < r/R < 1$, the gas volume fractions simulated with the oblate ellipsoidal bubble shape are higher than those simulated with the spherical bubble shape, which contributes to a better agreement between the simulation results and the experimental data.

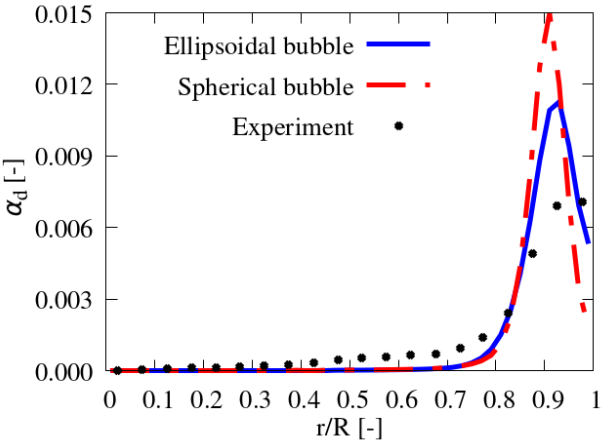

(a) MT20.

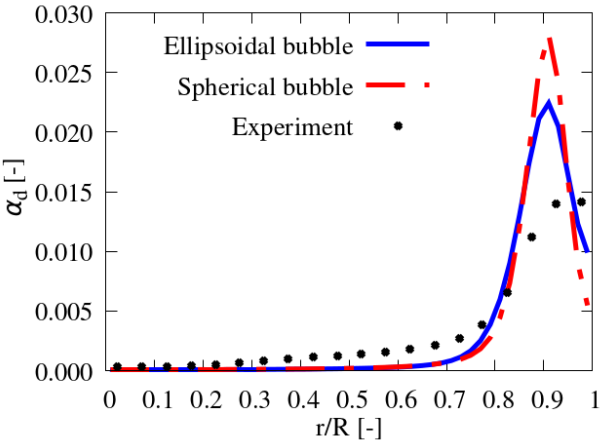

(b) MT42.

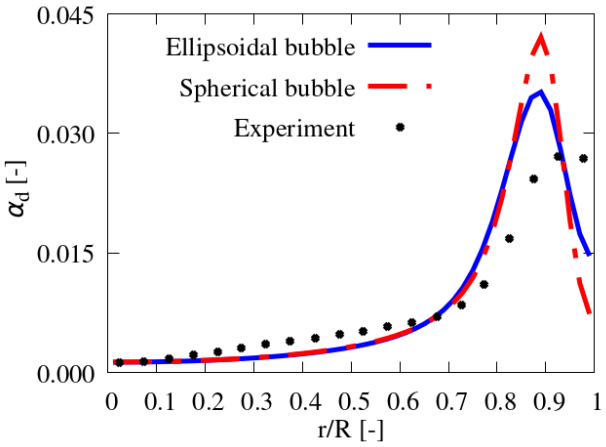

(c) MT64.

Figure 6: Gas volume fraction for monodisperse simulation with different bubble shapes.

The bubble shape effects on the axial gas velocity for the same simulations are shown in Fig. 7. The gas velocities simulated with both bubble shapes are approximately the same. The reason is that the effects of bubble deformation have been included in the drag force model used in the simulations for both bubble shapes. The simulated gas velocities for both bubble shapes agree well with the measurement data.

Figure 8 shows the gas volume fractions simulated with 4 bubble velocity groups and different bubble shapes in comparison with the experimental data. Herein, the results for case MT86 are presented. The results for cases MT42 and MT64 (not shown here) have a similar trend as case MT86. For case MT86, the peak of the total gas volume fraction profile simulated with the oblate ellipsoidal bubble shape is slightly lower than that simulated with the spherical bubble shape, but both of them are close to the peak in the experimental data. Near the wall with $0.92 < r/R < 1$, the total gas volume fraction simulated with the oblate ellipsoidal bubble shape is higher than that simulated with the spherical bubble shape. The difference in the simulated gas volume fractions originates from the results of the second bubble velocity group, which has a bubble size range of $3\,\text{mm} < d_B \leq 5.2\,\text{mm}$. For this bubble velocity group, the peak ratio of the gas volume fraction profiles is 1.36 for the spherical bubble shape. By contrast, the ratio decreases to 1.18 for the gas volume fraction simulated with the oblate ellipsoidal bubble shape. This proves that the over-prediction of the gas volume fraction peak near the wall is alleviated by considering the oblate ellipsoidal bubble shape in the simulations.

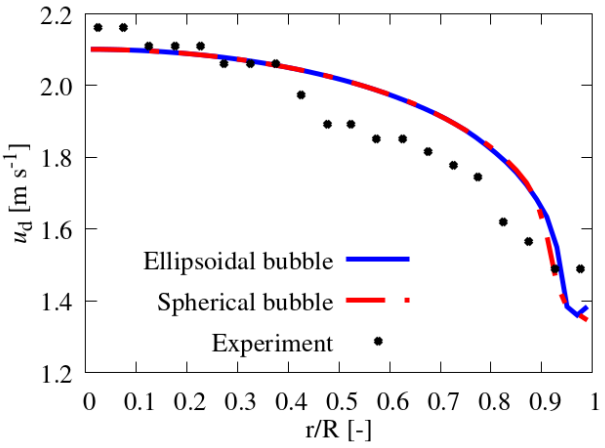

(a) MT20.

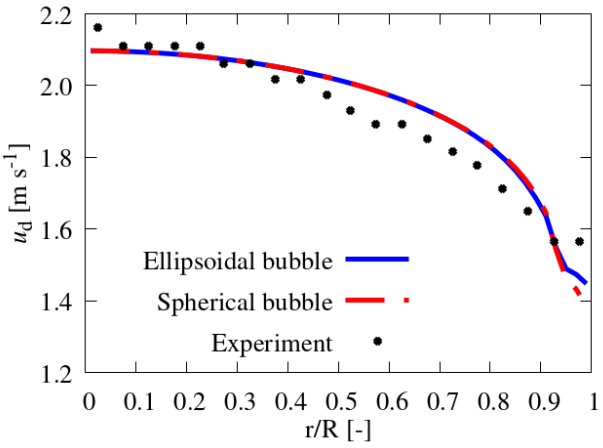

(b) MT42.

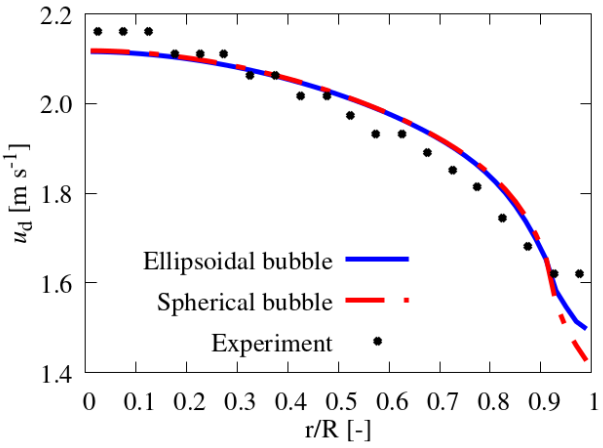

(c) MT64.

Figure 7: Axial gas velocity for monodisperse simulation with different bubble shapes.

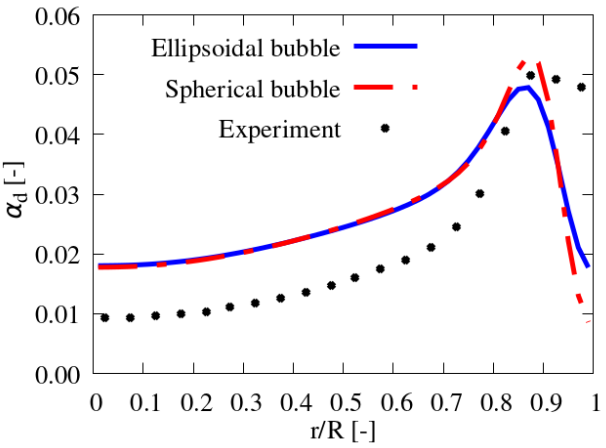

(a) Total gas volume fraction.

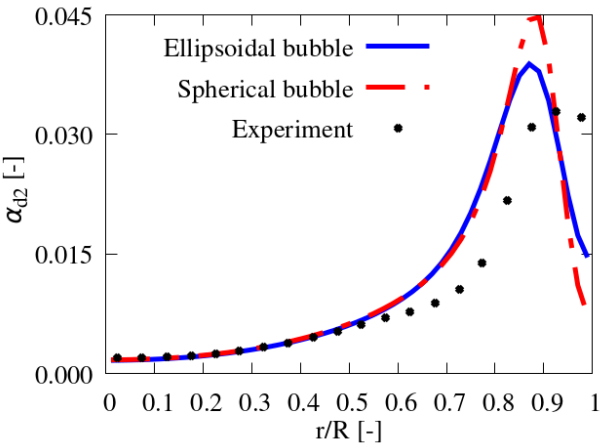

(b) Gas volume fraction of the 2nd bubble velocity group.

Figure 8: Gas volume fraction for case MT86 simulated with 4 bubble velocity groups and different bubble shapes.

5. Conclusion

For bubbly flow simulations with the Euler-Euler model, the small scales are not resolved. The interfacial momentum interactions and turbulence are represented by the closure models. Bubble size and shape are two important factors for the closure models. Assuming a constant bubble size for all the bubbles in simulations is not proper for polydisperse bubbly flows where the bubble size spectrum covers a wide range, especially when the bubble size spectrum crosses the critical bubble diameter of the shear-lift force changing its sign. An alternative way is to divide the bubbles in the system into different velocity groups and each velocity group has its size and velocity. In this way, the bubbles of different velocity groups can move in different directions.

This study has further developed and validated the particle-center-averaged Euler-Euler model for fixed polydisperse simulations. A comparison has been made for experimental data of bubbly pipe flows and the results simulated with the particle-center-averaged Euler-Euler model and the standard Euler-Euler model. The gas volume fraction simulated with the standard Euler-Euler model is more sensitive to the number of the bubble velocity groups than the particle-center-averaged Euler-Euler model. Moreover, for the standard Euler-Euler simulation, over-prediction of the gas volume fraction peak, which does not exist in a monodisperse simulation, can appear in a fixed polydisperse simulation.

The reason for these phenomena is that for the standard Euler-Euler model, the over-prediction is caused by the bubble force and the magnitude of the bubble forces changes after changing the number of bubble velocity groups. The bubble forces are functions of the local gas volume fraction. Hence, the forces can transport the gas to the peak without considering the bubble spatial extension when the bubble diameter is larger than the computational cell spacing. This leads to the over-prediction of the gas volume fraction peak. After changing the bubble forces to be functions of the bubble number density with the particle-center-averaging method, the over-prediction of the gas volume fraction peak is alleviated. The validation results of the particle-center-averaged Euler-Euler model also prove that assigning an individual bubble number density to each bubble velocity group works well for fixed polydisperse simulations and improves the predictions of the numerical simulation.

In the standard Euler-Euler model, the bubble deformation cannot directly influence the gas volume fraction distribution. It works by changing the effects of the closure models. As an advantage, in the particle-center-averaged Euler-Euler model, bubble deformation can directly influence the calculated gas volume fraction because it can be considered in the conversion between the bubble number density and the gas volume fraction. Based on this freedom, this study has introduced an anisotropic diffusion to consider the oblate ellipsoidal bubble shape in simulations. The bubble shape effects on the simulation results of bubbly flows in a vertical pipe have been investigated. The comparison between the simulation results and the measurement data illustrates that considering the oblate ellipsoidal bubble shape in simulations can alleviate the over-prediction of the gas volume fraction peak near the wall.

In the future, the particle-center-averaged Euler-Euler model can be coupled with the population balance model to consider the bubble coalescence and breakup for polydisperse bubbly flow simulations. Besides, the effects of zig-zag or spiral bubble movement on the gas volume fraction distribution can be investigated with the particle-center-averaged Euler-Euler model since the bubble influence region can be adjusted based on the bubble trajectories.

6. Acknowledgment

This work was supported by the China Scholarship Council (CSC) and partly supported by the Helmholtz European Partnering Program in the project “Crossing borders and scales (Crossing)”.

7. Nomenclature

Symbols

Symbol	Description	Unit
C_{diff}	diffusion coefficient	$\mathrm{m^2\,s^{-1}}$
$\mathbf{C}_{\mathrm{diff}}$	diffusion tensor	$\mathrm{m^2\,s^{-1}}$
$C_{\mathrm{diff,\,ij}}\,(i,j=x,y,z)$	diffusion tensor component	$\mathrm{m^2\,s^{-1}}$
d_{B}	bubble diameter	m
$d_{\mathrm{B}i}$	representative bubble diameter for the bubble velocity group i	m
Eo	Eötvös number	-
$\boldsymbol{f}$	force per unit volume	$\mathrm{N\,m^{-3}}$
$f_{\mathrm{v}i}$	volumetric flow rate fraction of the bubble velocity group i	-
$\boldsymbol{g}$	acceleration of gravity	$\mathrm{m\,s^{-2}}$
J	superficial velocity	$\mathrm{m\,s^{-1}}$
L	distance between bubble center and wall	m
n	number density of bubble centers	$\mathrm{m^{-3}}$
$\boldsymbol{n}_{\mathrm{w}}$	unit wall-normal vector pointing into the fluid	-
N_{g}	the number of the bubble velocity groups	-
p	pressure	$\mathrm{N\,m^{-2}}$
R	pipe radius	m
r	radial coordinate	m
$\mathbf{S}$	viscous stress tensor	$\mathrm{N\,m^{-2}}$
$\mathbf{T}$	Reynolds stress tensor	$\mathrm{N\,m^{-2}}$
t	physical time	s
$\boldsymbol{u}$	velocity vector	$\mathrm{m\,s^{-1}}$
u	axial velocity component	$\mathrm{m\,s^{-1}}$
$V_{\mathrm{B}i}$	representative bubble volume for the bubble velocity group i	$\mathrm{m^3}$
V_{e}	volume of a diffusion ellipsoid	$\mathrm{m^3}$
V_{s}	volume of a diffusion sphere	$\mathrm{m^3}$
x,y,z	spatial coordinates	m
$\boldsymbol{x}$, $\boldsymbol{x_0}$	spatial coordinate vector	m
α	volume fraction	-
$\beta_{\mathrm{d}i}$	gas volume fraction projecting all bubble volume to the bubble centers for the bubble velocity group i	-
ρ	density	$\mathrm{kg\,m^{-3}}$
$\Delta\rho$	density difference between continuous and disperse phase	$\mathrm{kg\,m^{-3}}$
σ	surface tension coefficient	$\mathrm{N\,m^{-1}}$
τ	diffusion pseudo-time	s
Φ	quantity	-
χ	aspect ratio of the oblate ellipsoidal bubble	-
Ω	fluid domain	$\mathrm{m^3}$

Symbols

Symbol	Description	Unit
$\overline{\cdot}$	phase-average	-
$< \cdot >$	particle-center-average	-
$\widetilde{\cdot}$	dimensionless	-

Subscripts

Subscript	Description
c	continuous
d	disperse
i	bubble velocity group i
max	maximum

Superscripts

Superscript	Description
WC	wall-contact force
sim	simulation
exp	experiment

References

Auton, T., Hunt, J., Prud'Homme, M., 1988. The force exerted on a body in inviscid unsteady non-uniform rotational flow. Journal of Fluid Mechanics 197, 241–257.

Basser, P.J., 1995. Inferring microstructural features and the physiological state of tissues from diffusion-weighted images. NMR in Biomedicine 8, 333–344.

Burns, A.D., Frank, T., Hamill, I., Shi, J.M., 2004. The Favre averaged drag model for turbulent dispersion in Eulerian multi-phase flows, in: 5th International Conference on Multiphase Flow, Yokohama, Japan. May 30–June 4.

Drew, D.A., 1983. Mathematical modeling of two-phase flow. Annual Review of Fluid Mechanics 15, 261–291.

Drew, D.A., Passman, S.L., 1998. Theory of multicomponent fluids. Springer.

Grace, J., Wairegi, T., TH, N., 1976. Shapes and velocities of single drops and bubbles moving freely through immiscible liquids. Transactions of the Institution of Chemical Engineers 54, 167–173.

Hänsch, S., Evdokimov, I., Schlegel, F., Lucas, D., 2021. A workflow for the sustainable development of closure models for bubbly flows. Chemical Engineering Science 244, 116807.

Hessenkemper, H., Ziegenhein, T., Rzehak, R., Lucas, D., Tomiyama, A., 2021. Lift force coefficient of ellipsoidal single bubbles in water. International Journal of Multiphase Flow 138, 103587.

Hosokawa, S., Tomiyama, A., Misaki, S., Hamada, T., 2002. Lateral migration of single bubbles due to the presence of wall, in: ASME Fluids Engineering Division Summer Meeting, Montreal, Canada. July 14-18.

Ishii, M., Hibiki, T., 2011. Thermo-fluid dynamics of two-phase flow. Springer Science & Business Media.

Ishii, M., Zuber, N., 1979. Drag coefficient and relative velocity in bubbly, droplet or particulate flows. AIChE journal 25, 843–855.

Jeong, H., Park, H., 2015. Near-wall rising behaviour of a deformable bubble at high Reynolds number. Journal of Fluid Mechanics 771, 564–594.

Liao, Y., Rzehak, R., Lucas, D., Krepper, E., 2015. Baseline closure model for dispersed bubbly flow: Bubble coalescence and breakup. Chemical Engineering Science 122, 336–349.

Lucas, D., Krepper, E., Prasser, H.M., 2005. Development of co-current air–water flow in a vertical pipe. International Journal of Multiphase Flow 31, 1304–1328.

Lucas, D., Krepper, E., Prasser, H.M., 2007. Use of models for lift, wall and turbulent dispersion forces acting on bubbles for poly-disperse flows. Chemical Engineering Science 62, 4146–4157.

Lucas, D., Tomiyama, A., 2011. On the role of the lateral lift force in poly-dispersed bubbly flows. International Journal of Multiphase Flow 37, 1178–1190.

Lyu, H., 2022. 3D-Euler-Euler modeling of adiabatic poly-disperse bubbly flows based on particle-center-averaging method. Ph.D. thesis. Technische Universität Dresden.

Lyu, H., Lucas, D., Rzehak, R., Schlegel, F., 2022. A particle-center-averaged Euler-Euler model for monodisperse bubbly flows. Chemical Engineering Science , 117943.

Lyu, H., Schlegel, F., Rzehak, R., Lucas, D., 2020. Improvement of Euler-Euler simulation of two-phase flow by particle-center-averaged method, in: 14th International Conference on CFD in 6 Oil & Gas, Metallurgical and Process Industries SINTEF, Trondheim, Norway, October 12–14, 2020, SINTEF Academic Press.

Ma, T., Santarelli, C., Ziegenhein, T., Lucas, D., Fröhlich, J., 2017. Direct numerical simulation–based Reynolds-averaged closure for bubble-induced turbulence. Physical Review Fluids 2, 034301.

Menter, F.R., 2009. Review of the shear-stress transport turbulence model experience from an industrial perspective. International Journal of Computational Fluid Dynamics 23, 305–316.

Painter, K., Hillen, T., 2013. Mathematical modelling of glioma growth: the use of Diffusion Tensor Imaging (DTI) data to predict the anisotropic pathways of cancer invasion. Journal of Theoretical Biology 323, 25–39.

Prasser, H., Lucas, D., Krepper, E., Baldauf, D., Böttger, A., Rohde, U., Schütz, P., Zippe, F., Zippe, W., Zschau, J., 2003. Flow maps and models for transient two-phase flows. Technical Report. Forschungszentrum Rossendorf e.V.

Prosperetti, A., 1998. Ensemble averaging techniques for disperse flows, in: Drew, D.A., Joseph, D.D., Passman, S.L. (Eds.), Particulate Flows. Springer, pp. 99–136.

Rzehak, R., Ziegenhein, T., Kriebitzsch, S., Krepper, E., Lucas, D., 2017. Unified modeling of bubbly flows in pipes, bubble columns, and airlift columns. Chemical Engineering Science 157, 147–158.

Sun, R., Xiao, H., 2015. Diffusion-based coarse graining in hybrid continuum–discrete solvers: Theoretical formulation and a priori tests. International Journal of Multiphase Flow 77, 142–157.

The OpenFOAM Foundation Ltd., 2021. OpenFOAM-dev. `https://github.com/OpenFOAM/OpenFOAM-dev/tree/de9b29f0fdbb176cc31b8d466f60be3f4fb934de`, commit on 24. March 2021.

Tomiyama, A., Tamai, H., Zun, I., Hosokawa, S., 2002. Transverse migration of single bubbles in simple shear flows. Chemical Engineering Science 57, 1849–1858.

Ziegenhein, T., Lucas, D., 2019. The critical bubble diameter of the lift force in technical and environmental, buoyancy-driven bubbly flows. International Journal of Multiphase Flow 116, 26–38.